ACS APPLIED ELECTRONIC MATERIALS

pubs.acs.org/acsaelm Article

Evidencing Dissipation Dilution in Large-Scale Arrays of Single-Layer WSe_2 Mechanical Resonators

Michael Pitts, Matthew Feuer, Anthony K. C. Tan, Alejandro R.-P. Montblanch, James Kerfoot, Evgeny M. Alexeev, Michael Högen, Patrick Hays, Seth A. Tongay, Andrea C. Ferrari, Mete Atatüre, and Dhiren M. Kara*

Cite This: ACS Appl. Electron. Mater. 2024, 6, 7898−7905 Read Online

ACCESS | Metrics & More | Article Recommendations | Supporting Information

ABSTRACT: Micromechanical resonators with very low mass are highly desirable for sensing and transduction applications. Layered materials (LMs) can be used to fabricate single- to few-atom thick suspended membranes, representing the ultimate limit to low mass. Transition-metal dichalcogenides (TMDs), such as WSe_2, are particularly compelling because they can host spatially confined excitons in single layer (1L), potentially enabling the creation of nonclassical mechanical states and interconnects between quantum networks and processors. However, these exciting prospects have been tempered by low device yields, invasive methods for detecting resonator motion, and high mechanical damping. Here, we report the creation of mechanical resonators by suspending 1L-WSe_2 across a 90 × 90 array of 2.5-μm diameter holes with a > 75% success rate. We detect the resonator room-temperature (RT) Brownian motion and measure resonator mass to quantify contamination, using below-bandgap laser interferometry. We investigate the relation between frequency, diameter, and mechanical quality factor, which can exceed 1000 in our devices. We find the dependence agrees with the effect of dissipation dilution, highlighting the importance of reducing mechanical mode-bending. Key to this is the large-scale, high-quality arrays that make it possible to access a frequency range that surpasses previous works. Further, the ability to fabricate large numbers of 1L resonators, and the simplicity of probing their motion without electrodes or an underlying reflective substrate, facilitates previously hard-to-reach configurations, such as resonators in phononic crystals or within optical cavities.

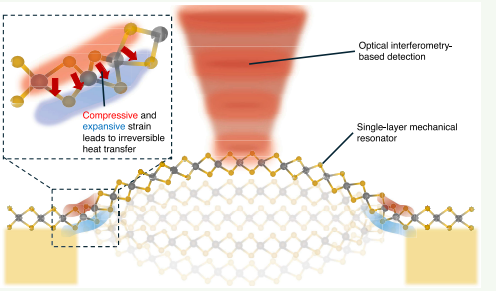

KEYWORDS: *layered materials, transition-metal dichalcogenide, mechanical resonators, quality factor, WSe_2, dissipation dilution*

INTRODUCTION

Solid-state micromechanical devices offer a range of applications including inertial navigation,[1] sensing,[2−4] GHz-bandwidth electro-optical modulation,[5] transduction of quantum information,[6−10] and the study of macroscopic objects in the quantum regime.[11−18] A particularly important metric for such devices is the mechanical Q-factor, Q_F, defined as $f_R/\Delta f$, where f_R and Δf is the resonance frequency and full-width at half-maximum (FWHM), respectively. Q_F determines the maximum attainable signal-to-noise ratio in sensing devices[19] and the phonon coherence time in quantum devices.[14] With improved fabrication techniques[20] and a deeper theoretical understanding of phonon losses,[21] there has been a pronounced increase of Q_F in Si-based resonators from thousands in the 1980s[22] to the billions that are now readily seen.[23−26] This has been achieved through the combined use of phononic crystal bandgaps, which reduce radiative losses of phonons to the resonator's supporting structure, and dissipation dilution via soft-clamping[14] and prestressing[21,27] the material, both of which reduce bending loss. During mechanical bending one side of the material is compressed and the other expands, creating a local temperature gradient. This results in heat transfer and, consequently, mechanical energy is lost from the resonator as it bends back and forth during oscillation.[21,27]

Layered materials (LMs), such as transition-metal dichalcogenides (TMDs) and graphene,[28] are a complementary platform to bulk materials for building mechanical resonators.[29−31] They can provide intrinsic opto-electrical activity,[32] and can be used to fabricate resonators with extremely low surface densities <10^{-5} kg/m^2,[33] compared to ∼10^{-4} kg/m^2 for some of the thinnest (∼30 nm) Si_3N_4 resonators.[23,34] The resulting low masses, on the order of femtograms for micron-scale devices, enhance sensitivity to parameters such as pressure, acceleration and adsorbed mass.[35,36] In the context of quantum technology, where mechanical systems have been

Received: July 18, 2024
Revised: September 9, 2024
Accepted: October 21, 2024
Published: November 11, 2024

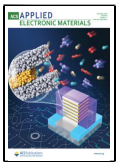

https://doi.org/10.1021/acsaelm.4c01261
ACS Appl. Electron. Mater. 2024, 6, 7898−7905

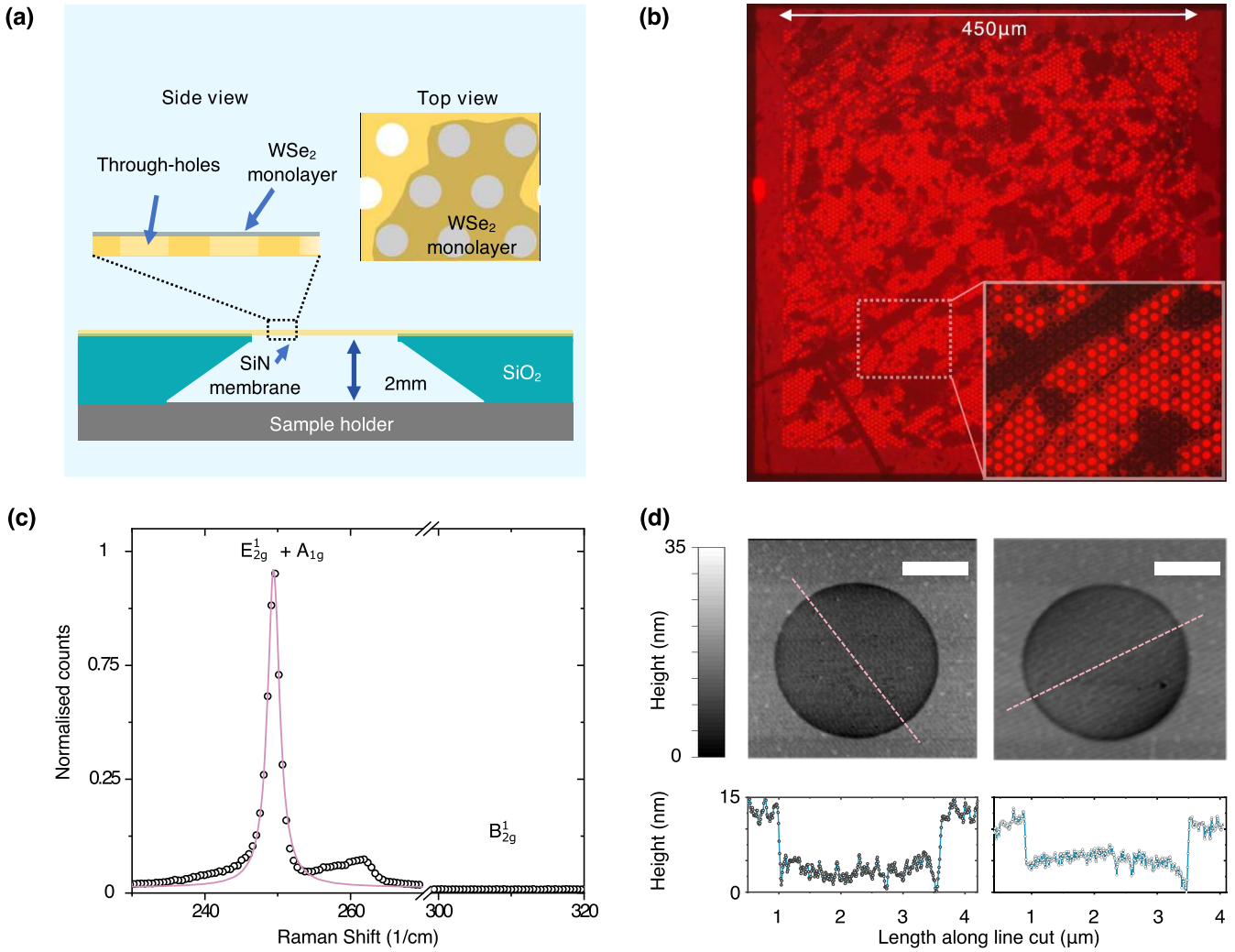

Figure 1. Suspended 1L-WSe_2 drum-head resonators. (a) Schematic of LM resonators prepared by placing 1L-WSe_2 onto a holey Si_3N_4 membrane. (b) RT PL image from 1L-WSe_2 flake on a 450 × 450 μm^2 grid of 2.5 μm diameter holes. The bright red circles in the magnified inset are suspended 1L-WSe_2 resonators. (c) Raman spectrum from a suspended resonator, fitted to a Lorentzian peak. (d) AFM image of two resonators, with line-cuts along the dashed lines of each given below. Scale bar: 1 μm.

proposed as interconnects between solid-state quantum processors and optical quantum networks,[37] the lower mass can offer increased coupling among phonons, photons, and electronic degrees of freedom, such as spin.[38] Despite these attractive properties, the best Q_F's reported for TMD resonators at room temperature (RT) are ~200[39] and up to ~1000 for multilayers.[39] There are orders of magnitude lower than silicon-based resonators, which have Q_F's in the ~10^6–10^{10} range for string, drum and trampoline configurations.[25,26,40−42]

The loss mechanisms associated with the low Q_F values of LM devices remain unidentified.[30] This is because LM resonators are difficult to produce in high numbers (hundreds) and with controlled properties, such as thickness or strain, necessary for systematic studies. Also, typical schemes required to detect motion of LMs, can restrict the geometry of devices and can be relatively invasive. For instance, the common method of capacitive detection can lead to current flow and Joule heating of the resonators. These problems make it difficult to distinguish the impact of one physical mechanism over another on resonator Q_F.

Here, we study 1L-WSe_2 resonators. These have interesting prospects for opto-mechanical coupling in the quantum regime, because 1L-WSe_2 can host excitons,[43] and single-photon emitters.[32] We combine Au assisted exfoliation[44] and polymer transfer[45] to create multiple 1L-WSe_2 micromechanical drumhead resonators on one substrate. For the first time we demonstrate detection of thermal (or Brownian) motion at RT of 1L-WSe_2 with laser light interferometry. We operate at 795 nm, below the bandgap of WSe_2 ≈ 760 nm.[46] This is important for reducing absorption induced heating and enables separate control of motion and excitons. We characterize over 50 resonators and observe a Q_F scaling on size and frequency, showing that for our 1L devices, bending losses dominate, rather than substrate coupling or surface dissipation. This motivates the development of methods to fabricate resonators with high strain for next-generation devices.

RESULTS AND DISCUSSION

We transfer 1L-WSe_2 onto 200 nm thick Si_3N_4 membranes with an array of through-holes, resulting in fully suspended 1L-WSe_2 mechanical resonators as shown in Figure 1a. Figure 1b is a photoluminescence (PL) image of 1L-WSe_2 placed on a

https://doi.org/10.1021/acsaelm.4c01261
ACS Appl. Electron. Mater. 2024, 6, 7898−7905

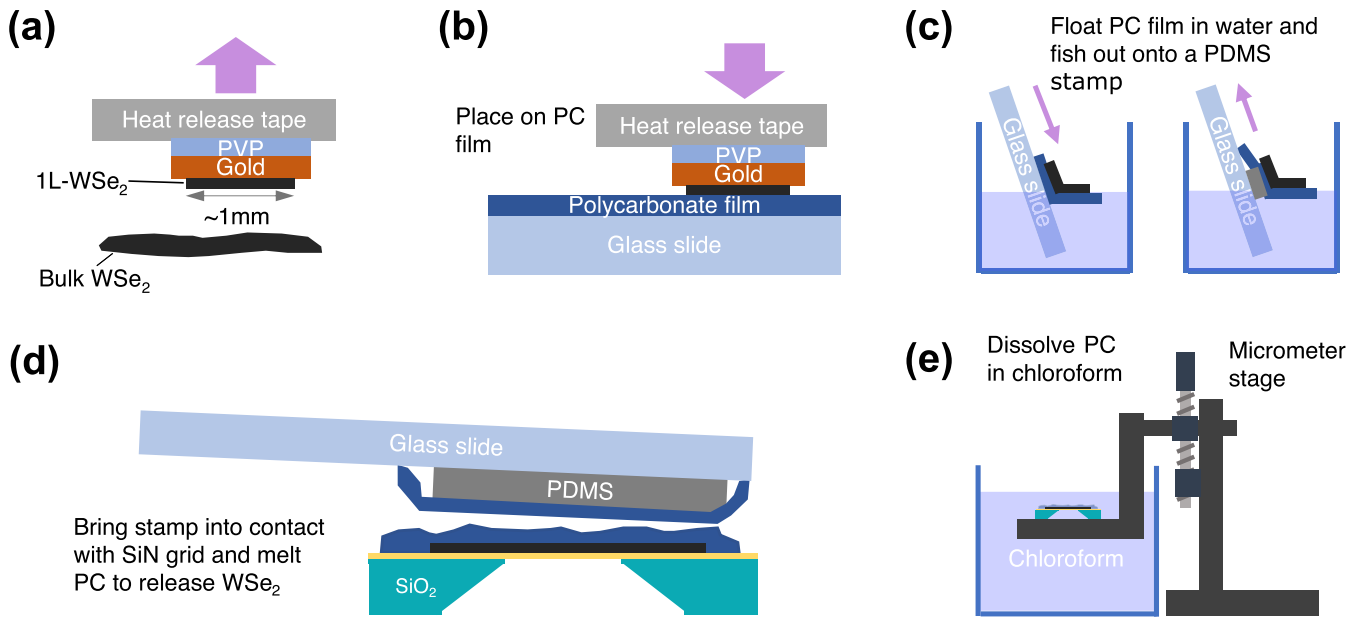

Figure 2. Schematic of steps for fabricating resonator arrays. (a) Au exfoliation of mm-scale 1L-WSe_2. (b) Transfer onto PC. (c) After removal of HRT/PVP/Au stack, the PC/WSe_2 is floated on water and fished out with a PDMS stamp. (d) The PC/1L-WSe_2 is deposited onto the holey Si_3N_4 grid by melting the PC. (e) The PC is dissolved through submersion in chloroform.

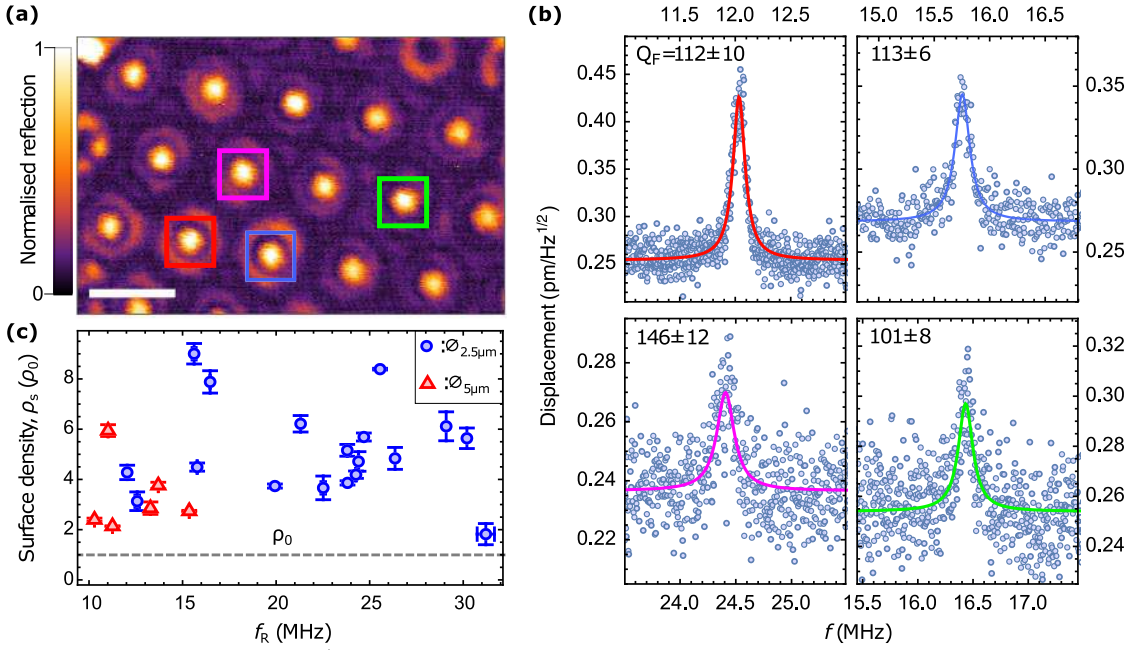

Figure 3. Thermal motion and mass of resonators. (a) Raster scan reflection image of 1L-WSe_2 on holey Si_3N_4, taken with a 795 nm-laser. Most holes are covered with suspended material, but two near the top right and far left are not and appear dark. Scale bar: 5 μm. (b) RT thermal motion of the fundamental mode of 4 resonators detected with optical interferometry. The solid-lines are Lorentzian fits (with an offset) and colored according to the resonator location as indicated by the squares in a. The quoted Q_F and uncertainties are means and standard errors, respectively, from 3 repeated measurements on each resonator. (c) Surface density of 24 resonators extracted from fits given in units of the theoretical surface density of pristine 1L-WSe_2, indicated with a dashed black line. Blue circles and red triangles correspond to 2.5 and 5 μm diameter resonators, respectively. The values and error bars are means and standard errors, respectively, from 3 repeated measurements on each resonator.

2.5 μm-diameter hole array of ~0.5 × 0.5 mm^2. The inset region is magnified by 2.5 times and suspended resonators appear as bright red circular regions. Broken drums or holes where no material is deposited appear black. The Si_3N_4-supported 1L-WSe_2 regions appear dimmer than the suspended ones with PL preferentially directed into the substrate, rather than toward the microscope objective, because of its higher refractive index (n_s = 2) in comparison to vacuum. 1L-WSe_2 drum-head resonators are suspended over 75% of the ~8000-hole membrane in Figure 1b, demonstrating the fabrication of thousands of resonators per fabrication run.

The 1L nature of the transferred WSe_2 is confirmed through the Raman spectrum in Figure 1c from a fully suspended region under 514 nm illumination. This has a characteristic

https://doi.org/10.1021/acsaelm.4c01261
ACS Appl. Electron. Mater. 2024, 6, 7898−7905

strong E_{2g} + A_{1g} peak at 249 cm^{-1} and an absence of the B^1_{2g} out-of-plane mode, which is present only for multilayers.[47] Further Raman characterization at various steps of the fabrication procedure are given in Supporting Note S1. Figure 1d is the surface topography of two resonators measured with atomic force microscopy (AFM) demonstrating that our method is capable of producing resonators free from patches of contamination and wrinkles. Supporting Note S2 provides further details of our AFM procedure and a 30 × 30 μm area scan. Height profiles across a line cut of the suspended 1L-WSe_2 in Figure 1d are given in the bottom panels and show a drop in height of the suspended regions compared to the Si_3N_4-supported areas, resulting from sidewall adhesion of 1L-WSe_2 to the substrate, as previously reported for suspended LMs.[48] We observe that the amount of adhesion varies between resonators across the sample (see also Supporting Figure S2), indicating different amounts of pretension introduced during fabrication. The periodic features in Figure 1d are an artifact of the gain settings of the AFM scanner and not a feature of the sample.

Fabrication of Resonator Arrays. Figure 2 highlights the key aspects of our resonator fabrication process (see Methods section for further details). To isolate mm-scale flakes of 1L-WSe_2, we take a stack of heat release tape (HRT)/poly(vinylpyrrolidone) (PVP)/200 nm-thick Au and bring it into contact with a bulk WSe_2 crystal. On retraction, 1L-WSe_2 is exfoliated (Figure 2a), due to the stronger van der Waals interaction between the Au surface and the exposed Se atoms of the first layer of WSe_2 in comparison to the Se−Se interaction in the bulk crystal.[49] The stack is then deposited onto a polycarbonate (PC) film on a glass slide (Figure 2b), and the HRT/PVP/Au stack is removed by sequential heating, deionized (DI) water cleaning, O_2 plasma etching and etching in aqueous KI solution. This approach consistently produces a 2 × 2 mm^2 area of 1L-WSe_2 on PC. Next, we float the PC/WSe_2 on the surface of DI water and onto poly(dimethylsiloxane) (PDMS) to create a stamp (Figure 2c). The PDMS/PC/1L-WSe_2 stamp is brought into contact with the Si_3N_4 substrate at a small angle (∼10°), which we find reduces wrinkling. The PC is then melted at 180 °C, depositing the PC/1L-WSe_2 onto Si_3N_4 (Figure 2d). In the final step, we dissolve the PC by submerging the PC/1L-WSe_2/Si_3N_4 in chloroform with a manual translation stage (Figure 2e) to reduce rupturing of the suspended 1L-WSe_2 regions. We use PC in the transfer process because it has been found to be more soluble than other transfer polymers,[50] such as poly(methyl methacrylate)[51] and PDMS,[52] which typically require a high-temperature anneal (>180 °C) to remove polymer residue.

Detection of Thermal Motion. To image resonators and to detect their motion interferometrically, we use laser-light of λ_L = 795 nm, focused with a 0.7 numerical aperture (NA) objective. Figure 3a is a 28 × 17 μm^2 raster-scanned reflection image of our sample taken with a custom-built confocal scanning microscope. The uncovered holes of the membrane appear dark and suspended resonators are resolved as regions of higher reflection. The Si_3N_4-supported 1L-WSe_2 areas also appear dark because λ_L is close to the antireflective condition of our substrate such that $\lambda_L \approx 2n_s t_s$, where n_s = 2 and t_s = 200 nm are the substrate refractive index and thickness, respectively.

We detect resonator motion by interfering the light reflected from the center of a resonator with that reflected from a piezoelectric-mounted mirror (PZTM), similar to the scheme in ref 53 we set the interferometer arm lengths to be equal within 50 mm and implement balanced detection of the interferometer fringes to suppress laser phase and amplitude noise, respectively. A schematic of the setup is given in Supporting Figure S3. The interferometer is locked to the side of a fringe via slow feedback ≲5 kHz to the PZTM. At this lock-point, the voltage output of our balanced detectors, V_{det}, is linearly dependent on small ($\ll\lambda_L$) resonator displacements, which occur in the frequency range 10−50 MHz. This means we can use self-calibration to convert the V_{det} spectral density, $S_v(f)$, into the resonator displacement spectral density, $S_z(f)$, where f is the signal frequency, through[54]

$$S_z(f) + S_n = \left(\frac{c_{opt}\lambda_l}{2\pi V_{det}^{pk-pk}}\right)^2 S_v(f) \quad (1)$$

where S_n indicates measurement imprecision and differs from one resonator to another, but is typically (∼250 fm/$Hz^{1/2}$)^2, spectrally flat, and originates from a combination of electrical noise from the photodiode detectors and optical shot-noise; V_{det}^{pk-pk} is the measured peak-to-peak voltage of our interference signal when actively driving the PZTM with amplitudes >λ_L and is dependent on the specific resonator and laser power used. The dimensionless factor, c_{opt}, accounts for the fact that $S_z(f)$ is defined for the point of maximum displacement of the resonator, whereas the laser has a finite spot size ∼0.5 μm. For our 2.5 μm drums c_{opt} = 1.23 (see Methods section for details).

Figure 3b plots the displacement of 4 undriven resonators measured in a vacuum of 10^{-6} mbar, where gas damping of the motion is negligible. The resonator locations are given by red, blue, pink and green squares in Figure 3a. Their thermal motion is resolved because of the low $S_n^{1/2}$ ∼250 fm/$Hz^{1/2}$ achieved with our interferometer, corresponding to the noise-floor of the displacement spectra in Figure 3b. These measurements are performed with low optical power, ∼0.1 mW at the resonator, such that the resonator frequency, f_R, and Q_F are unaffected by the detection laser (see Supporting Figure S4). The solid lines in Figure 3b are fits of $S_z(f)$ to the expected thermal motion spectral density:[54,55]

$$S_z^{thermal}(f) = \frac{k_B T}{2\pi^3 m_{eff} Q_F[(f^2 - f_R^2)^2 + (f f_R/Q_F)^2]} \quad (2)$$

with T = 290 K. From the fit we can extract not only the resonance frequency, f_R, and Q_F (indicated in Figure 3b), but also the effective masses, m_{eff}, of our resonators, related to the suspended mass m_s, through m_{eff} = 0.27 m_s for the fundamental mode.[54] Comparing the measured m_s to the expected pristine mass $\pi(\varnothing/2)^2\rho_0$, where $\varnothing$ is the resonator diameter and ρ_0 = 6.03 × 10^{-6} kg/m^2 (based on the 1L-WSe_2 lattice constant and atomic masses), provides an indicator of the resonator contamination. This is particularly important for LM devices, as contamination can significantly impact device performance, but is often difficult to measure and quantify.

Figure 3c shows the measured suspended mass density, ρ_s, in units of ρ_0, extracted from fitting the thermal motion for eighteen 2.5 μm (blue circles) and six 5 μm-diameter (red triangles) resonators. There is a distribution of 2−10ρ_0, and we attribute the extra mass to adsorbates or residue introduced during fabrication, such as Au and PC too small (<1 nm) to be seen in our AFM scans. The value of 2ρ_0 is comparable to previous works, including chemical vapor deposition grown

https://doi.org/10.1021/acsaelm.4c01261
ACS Appl. Electron. Mater. 2024, 6, 7898−7905

and PDMS exfoliated flakes,[30] and equates to effective masses ~10 fg. If the additional mass was the main cause of our mechanical resonator frequency distribution we would expect a correlation between f_R and $\rho_s^{1/2}$. Using the Pearson correlation coefficient,[56] C (see Methods section for definition), we find $C_{2.5\ \mu m}(f_R, \rho_s^{1/2}) = -0.12$ (3.s.f.) and $C_{5\ \mu m}(f_R, \rho_s^{1/2}) = -0.09$, indicating very weak to no correlation. This shows that the distribution of frequencies we measure for a given resonator diameter is not caused by a distribution of ρ_s, but rather the material strain. We also find that Q_F does not strongly correlate with ρ_s, with $C_{2.5\ \mu m}(Q_F, \rho_s) = -0.2$ and $C_{5\ \mu m}(Q_F, \rho_s) = -0.12$ indicating that contamination does not dominate mechanical losses (see Supporting Figure S5).

Evidence of Dissipation Dilution. Figure 4a plots f_R and Q_F of forty-two 2.5 μm-diameter resonators (blue circles) and nineteen 5 μm-diameter resonators (red triangles). The orange circles are 10 measurements from a second 2.5 μm-diameter device. These are comparable with our first device indicating the reproducibility of our results. Across all resonators we observe that a larger f_R (i.e., larger tension) results in a larger Q_F. Specifically, we plot our data on a quadratic-scale to highlight the linear dependence between f_R^2 and Q_F. This is consistent with the dissipation dilution effect[21] and is well-known in bulk resonators, where tensioning leads to an increase in the fraction of mechanical energy stored as lossless tensile energy versus lossy bending energy.[27] In the context of circular drum resonators, this behavior is tied to the distribution between membrane, W_{mem}, and plate, W_p, energies, for which the tension and material rigidity act as the restoring forces, respectively. The enhancement of Q_F scales as W_{mem}/W_p and follows $Q_F = af_R^2 + b$, where a and b are constants for a resonator of given dimensions.[21,30] A least-squares fit of this functional form is shown as a solid blue line for the 2.5 μm resonators, agreeing well with the data.

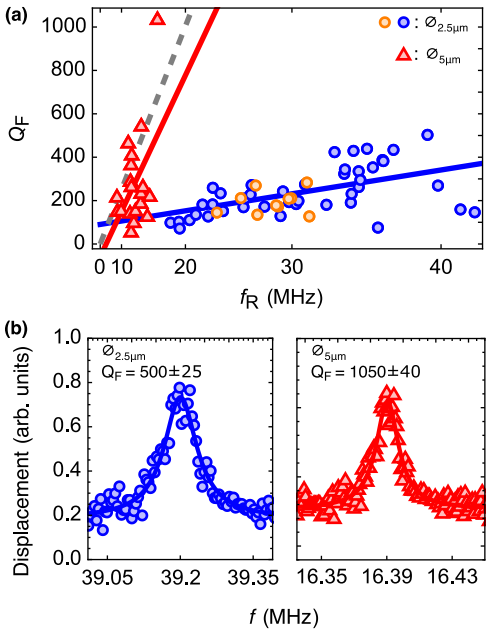

Figure 4. Increase of Q_F with resonator frequency and diameter. (a) Q_F for resonators across a range of f_R, plotted on a quadratic scale, for $\varnothing$'s 2.5 μm (blue circles) and 5 μm (red triangles), showing a trend of reduced damping for increased tension and drum diameter. The solid-line fits have the functional form $Q_F = af_R^2 + b$ with a values of 0.16 ± 0.04 and 2.1 ± 1 Hz^{2-}, for the 2.5 and 5 μm resonators, respectively, with a ratio of ~13. The consistency of the behavior and our fabrication method is shown by the orange circle data, which come from a second 2.5 μm device. The gray dashed line indicates the expected Q_F trend-line for 5 μm resonators based on the 2.5 μm data assuming bending losses dominate. The sample errors of Q_F values are 5−10% (not shown) and f_R are smaller than the point sizes. (b) Thermal motion resonance for the highest Q_F's measured for diameters 2.5 μm (blue circles) and 5 μm (red triangles).

Taking the ideal case, where bending occurs mainly at the clamping points of the resonator, and tension is uniform across the resonator, we would expect that doubling $\varnothing$ to 5 μm would lead to an increase in a by a factor $2^4 = 16$. This is because for a given resonator frequency, $W_{mem} \propto \varnothing^2$, whereas $W_p \propto \varnothing^{-2}$, such that $W_{mem}/W_p \propto \varnothing^4$.[21,30] The gray dashed line in Figure 4a is the predicted Q_F of 5 μm-diameter resonators based on the 2.5 μm-diameter resonator data. The red triangles in Figure 4a show that 5 μm resonators do result in higher Q_F, with the best fit line shown in solid red. The Q_F's are slightly less than the ideal predicted case, and this could be due to nonuniform strain across our resonators resulting from differences in sidewall adhesion or the potential role of damping mechanisms related to surface effects. We find that $C_{2.5\ \mu m}(f_R^2, Q_F) = 0.55$ and $C_{5\ \mu m}(f_R^2, Q_F) = 0.47$. These are reduced by only a small amount when controlling for ρ_s, with the partial coefficients (see Methods for further information) being $PC_{2.5\mu m}(f_R^2, Q_F|\rho_s) = 0.54$ and $PC_{5\mu m}(f_R^2, Q_F|\rho_s) = 0.46$. The strong correlations further support that Q_F is mainly governed by resonator strain.

The behavior of our resonators remains the same over time and after repeated mounting and unmounting of our samples from the vacuum chamber, with the data in Figure 4a coming from measurements across a 9 months period. Unmounted samples were stored in a nitrogen desiccator box. We note that an increase of Q_F with strain has been seen in multilayer MoS_2[57] and with size in graphene,[58] however the dependencies were not consistent with dissipation dilution.

The Brownian motion resonance corresponding to the highest Q_F measured is in Figure 4b for diameters 2.5 μm (blue circles) and 5 μm (red triangles). As we do not see saturation of our Q_F in Figure 4a, indicating that other loss mechanisms remain small, we can estimate an upper bound for the Q_F we would expect for a resonator fabricated with a pretension close to the yield tension of WSe_2, $L_{max} \sim 10$ N/m.[59] We use the relation $f_R = (2\pi\alpha_{01}/\varnothing)\sqrt{L/\rho_s}$, where $\alpha_{01} = 2.405$, to estimate that the pretension of our highest Q_F resonator is $L \approx 0.1$ N/m. Therefore, in the absence of any other loss mechanism becoming significant we would expect a maximum $Q_F^{max} \approx (10/0.1) \times 1050 \approx 10^5$ for a 5 μm resonator at RT.

CONCLUSIONS

We reported a method to reliably fabricate thousands of 1L-TMD resonators in a single processing run, and the detection of their RT thermal motion via optical reflection interferometry. These developments will allow further systematic studies of LM resonators with less restrictive device geometries, e.g., resonators deposited on substrates that have a phononic bandgap, embedded inside optical cavities, and the exploration of coupled TMD resonators. We utilized the statistical characterization afforded by the many tens of resonators we studied, to reveal that bending losses play an important role in damping. This strongly motivates the development of methods to strain engineer LM devices either through pretensioning

https://doi.org/10.1021/acsaelm.4c01261
ACS Appl. Electron. Mater. 2024, 6, 7898−7905

during fabrication, or via configurable substrates, and for suspending 1L material over larger areas. Addressing the problem of low Q_F's could open up new avenues in fundamental science that exploit the large zero-point motion and optoelectronic activity[32] of these single-layer TMD devices[36,37,60] and offer applications of utilizing TMDs that host spin-active quantum emitters as quantum interconnects and for quantum phononics.

METHODS

Fabrication. The Au film for exfoliation is made by taking a chemical-mechanical polished Si wafer and cleaning the surface in a reactive-ion-etch with oxygen plasma at 60 W for 1 min. It is then placed into an e-beam evaporator. The first 5 nm of Au are deposited at a rate of 0.1 Å/s and the next 195 nm at 2 Å/s. Next a layer of PVP is spin coated onto the surface at a rate of 3000 rpm and an acceleration of 1000 rpm/s for 2 min. After this, the wafer is baked for 5 min at 150 °C. The heat release tape used is Revalpha SEC P/N 21876 single sided, 90 °C heat release.

When Au is picked up from the Si wafer to make the heat release tape/PVP/Au stack, it must be pressed onto the WSe_2 as quickly as possible and then peeled off, as shown in Figure 2a. A PC film is made by taking a few drops of a 5% weight solution of PC in chloroform and putting these onto one glass slide and scraping another glass slide over the top to create a uniform layer which then dries. The heat release tape/PVP/Au/WSe_2 is pressed onto the PC film and the whole glass slide is placed onto a hot plate to remove the heat release tape at 110 °C. The PVP is dissolved by submerging the glass slide in DI water for 5 min. Au is removed by placing the glass slide in Au standard etchant for 1 min, followed by cleaning in a DI water bath for 20 min and in ethanol for 5 min. The 1L-WSe_2-coated PC segment is then cut out, floated and fished out onto a square of PDMS, as in Figure 2b. Finally the 1L-WSe_2 is transferred onto the Si_3N_4 grid (PELCO Holey Silicon Nitride Support Film) to make resonators and cleaned in chloroform, as shown in Figure 2c,d.

Interferometer Calibration. Equation 1 allows us to convert the measured interferometer power spectrum $S_v(f)$ into resonator displacement $S_z(f)$, defined for the position of maximum displacement (coincident with the center of the drum for the fundamental mode). The factor c_{opt} in eq 1 accounts for the fact that the laser has a finite spot-size at the resonator, and therefore also samples regions away from the maximum displacement. c_{opt} depends on the resonator diameter, d, the laser profile at the sample, $I(r)$, and the displacement profile of the fundamental mechanical mode, $M(r)$, where r is the distance from the center of the resonator, as follows:

$$c_{opt} = \frac{\int_0^{d/2} I(r)M(0)r\mathrm{d}r}{\int_0^{d/2} I(r)M(r)r\mathrm{d}r} \tag{3}$$

We measure the laser profile with a knife-edge profiler to be $I(r) = I_0 e^{-2r/\omega_0}$ with $\omega_0 = 675$ nm, and we take the standard solution to a vibrating drum-membrane, $M(r) = J_0(\alpha_{01} r/(\varnothing/2))$, where J_0 is the first-order Bessel function of the first kind and $\alpha_{01} = 2.405$(3.d.p) such that $J_0(\alpha_{01}) = 0$. For our 2.5 and 5 μm-diameter drums, $c_{opt} = 1.23$ and 1.05, respectively.

Definition of Correlation Function. To determine the correlation and partial correlations coefficients given in the main text we use the Pearson correlation[56] defined as:

$$C(X, Y) = \frac{\sum_{i=1}^{n}(x_i - \overline{x})(y_i - \overline{y})}{\sqrt{\sum_{i=1}^{n}(x_i - \overline{x})^2}\sqrt{\sum_{i=1}^{n}(y_i - \overline{y})^2}}$$

$$PC(X, Y|Z) = \frac{C(X, Y) - C(X, Z)C(Y, Z)}{\sqrt{1 - C(X, Z)^2}\sqrt{1 - C(Y, Z)^2}}$$

where x_i and y_i are individual data points, and $\overline{x}$ and $\overline{y}$ are the mean values, of X and Y each of length n, respectively. Z is the data (or variable) that is being controlled for. The coefficients can take values $-1 < C(X,Y), PC(X,Y|Z) < +1$, with values +1 and −1 corresponding to perfect positive and negative correlation, respectively, and 0 no correlation.

ASSOCIATED CONTENT

Supporting Information

The Supporting Information is available free of charge at https://pubs.acs.org/doi/10.1021/acsaelm.4c01261.

Raman and PL spectroscopy of layered material; atomic force microscopy image of suspended 1L−WSe_2; diagram of interferometer setup; independence between Q_F and ρ_s (PDF)

AUTHOR INFORMATION

Corresponding Author

Dhiren M. Kara − *Center for Macroscopic Quantum States (bigQ), Department of Physics, Technical University of Denmark, 2800 Kongens Lyngby, Denmark;* orcid.org/0000-0003-1052-5495; Email: dhika@dtu.dk

Authors

Michael Pitts − *Cavendish Laboratory, University of Cambridge, Cambridge CB3 0HE, U.K.; Cambridge Graphene Centre, University of Cambridge, Cambridge CB3 0FA, U.K.*

Matthew Feuer − *Cavendish Laboratory, University of Cambridge, Cambridge CB3 0HE, U.K.*

Anthony K. C. Tan − *Cavendish Laboratory, University of Cambridge, Cambridge CB3 0HE, U.K.*

Alejandro R.-P. Montblanch − *Quantum Technologies Group, Emerging Technology, Innovation & Ventures, HSBC Lab, E14 5HQ London, U.K.*

James Kerfoot − *Cambridge Graphene Centre, University of Cambridge, Cambridge CB3 0FA, U.K.;* orcid.org/0000-0002-6041-4833

Evgeny M. Alexeev − *Cambridge Graphene Centre, University of Cambridge, Cambridge CB3 0FA, U.K.; Cavendish Laboratory, University of Cambridge, Cambridge CB3 0HE, U.K.;* orcid.org/0000-0002-8149-6364

Michael Högen − *Cavendish Laboratory, University of Cambridge, Cambridge CB3 0HE, U.K.*

Patrick Hays − *Materials Science and Engineering, School for Engineering of Matter, Transport and Energy, Arizona State University, Tempe, Arizona 85287, United States*

Seth A. Tongay − *Materials Science and Engineering, School for Engineering of Matter, Transport and Energy, Arizona State University, Tempe, Arizona 85287, United States;* orcid.org/0000-0001-8294-984X

Andrea C. Ferrari − *Cambridge Graphene Centre, University of Cambridge, Cambridge CB3 0FA, U.K.*

Mete Atatüre − *Cavendish Laboratory, University of Cambridge, Cambridge CB3 0HE, U.K.;* orcid.org/0000-0003-3852-0944

Complete contact information is available at: https://pubs.acs.org/10.1021/acsaelm.4c01261

Notes

The authors declare no competing financial interest.

Disclaimer This paper was prepared for information purposes and is not a product of HSBC Bank Plc. or its affiliates. Neither HSBC Bank Plc. nor any of its affiliates make any explicit or implied representation or warranty, and none of them accept

https://doi.org/10.1021/acsaelm.4c01261
ACS Appl. Electron. Mater. 2024, 6, 7898−7905

■ ACKNOWLEDGMENTS

We acknowledge funding from a Royal Society university research fellowship URF\R1\180593, the EU Quantum Technology (2D-SIPC) and Graphene Flagships; EU grants CHARM and Graph-X; ERC grants PEGASOS, Hetero2D and GSYNCOR; and EPSRC Grants EP/K01711X/1, EP/K017144/1, EP/N010345/1 and EP/L016087/1. S. T. acknowledges primary support from DOE-SC0020653 (materials synthesis), Applied Materials Inc., DMR 2111812 (materials characterization/optimization), DMR 2206987 (impurity tests), CMMI 2129412 (manufacturing) and partial support from Lawrence Semiconductor Laboratories.

■ REFERENCES

(1) Yazdi, N.; Ayazi, F.; Najafi, K. Micromachined inertial sensors. *Proc. IEEE* **1998**, *86*, 1640−1659.
(2) Binnig, G.; Quate, C. F.; Gerber, C. Atomic force microscope. *Phys. Rev. Lett.* **1986**, *56*, 930−933.
(3) Ekinci, K. L.; Yang, Y. T.; Roukes, M. L. Ultimate limits to inertial mass sensing based upon nanoelectromechanical systems. *J. Appl. Phys.* **2004**, *95*, 2682−2689.
(4) Naik, A. K.; Hanay, M. S.; Hiebert, W. K.; Feng, X. L.; Roukes, M. L. Towards single-molecule nanomechanical mass spectrometry. *Nat. Nanotechnol.* **2009**, *4*, 445−450.
(5) Haffner, C.; Joerg, A.; Doderer, M.; Mayor, F.; Chelladurai, D.; Fedoryshyn, Y.; Roman, C. I.; Mazur, M.; Burla, M.; Lezec, H. J.; Aksyuk, V. A.; Leuthold, J. Nano−opto-electro-mechanical switches operated at CMOS-level voltages. *Science* **2019**, *366*, 860−864.
(6) Kurizki, G.; Bertet, P.; Kubo, Y.; Mølmer, K.; Petrosyan, D.; Rabl, P.; Schmiedmayer, J. Quantum technologies with hybrid systems. *Proc. Natl. Acad. Sci. U.S.A.* **2015**, *112*, 3866−3873.
(7) Chu, Y.; Kharel, P.; Yoon, T.; Frunzio, L.; Rakich, P. T.; Schoelkopf, R. J. Creation and control of multi-phonon Fock states in a bulk acoustic-wave resonator. *Nature* **2018**, *563*, 666−670.
(8) Bienfait, A.; Satzinger, K. J.; Zhong, Y. P.; Chang, H. S.; Chou, M. H.; Conner, C. R.; Dumur; Grebel, J.; Peairs, G. A.; Povey, R. G.; Cleland, A. N. Phonon-mediated quantum state transfer and remote qubit entanglement. *Science* **2019**, *364*, 368−371.
(9) Mirhosseini, M.; Sipahigil, A.; Kalaee, M.; Painter, O. Superconducting qubit to optical photon transduction. *Nature* **2020**, *588*, 599−603.
(10) Clerk, A. A.; Lehnert, K. W.; Bertet, P.; Petta, J. R.; Nakamura, Y. Hybrid quantum systems with circuit quantum electrodynamics. *Nat. Phys.* **2020**, *16*, 257−267.
(11) O'Connell, A. D.; Hofheinz, M.; Ansmann, M.; Bialczak, R. C.; Lenander, M.; Lucero, E.; Neeley, M.; Sank, D.; Wang, H.; Weides, M.; Wenner, J.; Martinis, J. M.; Cleland, A. N. Quantum ground state and single-phonon control of a mechanical resonator. *Nature* **2010**, *464*, 697−703.
(12) Chan, J.; Alegre, T. P.; Safavi-Naeini, A. H.; Hill, J. T.; Krause, A.; Gröblacher, S.; Aspelmeyer, M.; Painter, O. Laser cooling of a nanomechanical oscillator into its quantum ground state. *Nature* **2011**, *478*, 89−92.
(13) Teufel, J. D.; Donner, T.; Li, D.; Harlow, J. W.; Allman, M. S.; Cicak, K.; Sirois, A. J.; Whittaker, J. D.; Lehnert, K. W.; Simmonds, R. W. Sideband cooling of micromechanical motion to the quantum ground state. *Nature* **2011**, *475*, 359−363.
(14) Rossi, M.; Mason, D.; Chen, J.; Tsaturyan, Y.; Schliesser, A. Measurement-based quantum control of mechanical motion. *Nature* **2018**, *563*, 53−58.
(15) Fröwis, F.; Sekatski, P.; Dür, W.; Gisin, N.; Sangouard, N. Macroscopic quantum states: Measures, fragility, and implementations. *Rev. Mod. Phys.* **2018**, *90*, No. 025004.
(16) Riedinger, R.; Wallucks, A.; Marinković, I.; Löschnauer, C.; Aspelmeyer, M.; Hong, S.; Gröblacher, S. Remote quantum entanglement between two micromechanical oscillators. *Nature* **2018**, *556*, 473−477.
(17) Ockeloen-Korppi, C. F.; Damskägg, E.; Pirkkalainen, J.-M.; Asjad, M.; Clerk, A. A.; Massel, F.; Woolley, M. J.; Sillanpää, M. A. Stabilized entanglement of massive mechanical oscillators. *Nature* **2018**, *556*, 478−482.
(18) Qiu, L.; Shomroni, I.; Seidler, P.; Kippenberg, T. J. Laser Cooling of a Nanomechanical Oscillator to Its Zero-Point Energy. *Phys. Rev. Lett.* **2020**, *124*, No. 173601.
(19) Schmid, S.; Villanueva, L.; Roukes, M. *Fundamentals of Nanomechanical Resonators*; Springer International Publishing, 2023.
(20) Kaloyeros, A. E.; Pan, Y.; Goff, J.; Arkles, B. Review—Silicon Nitride and Silicon Nitride-Rich Thin Film Technologies: State-of-the-Art Processing Technologies, Properties, and Applications. *ECS J. Solid State Sci. Technol.* **2020**, *9*, No. 063006.
(21) Sementilli, L.; Romero, E.; Bowen, W. P. Nanomechanical Dissipation and Strain Engineering. *Adv. Funct. Mater.* **2022**, *32*, No. 2105247.
(22) Tudor, M.; Andrés, M. V.; Foulds, K.; Naden, J. Silicon resonator sensors: interrogation techniques and characteristics. *IEE Proc.-D: Control Theory Appl.* **1988**, *135* (5), 364−368.
(23) Tsaturyan, Y.; Barg, A.; Polzik, E. S.; Schliesser, A. Ultracoherent nanomechanical resonators via soft clamping and dissipation dilution. *Nat. Nanotechnol.* **2017**, *12*, 776−783.
(24) Ghadimi, A. H.; Fedorov, S. A.; Engelsen, N. J.; Bereyhi, M. J.; Schilling, R.; Wilson, D. J.; Kippenberg, T. J. Elastic strain engineering for ultralow mechanical dissipation. *Science* **2018**, *360*, 764−768.
(25) Høj, D.; Wang, F.; Gao, W.; Hoff, U. B.; Sigmund, O.; Andersen, U. L. Ultra-coherent nanomechanical resonators based on inverse design. *Nat. Commun.* **2021**, *12*, No. 5766.
(26) Beccari, A.; Visani, D. A.; Fedorov, S. A.; Bereyhi, M. J.; Boureau, V.; Engelsen, N. J.; Kippenberg, T. J. Strained crystalline nanomechanical resonators with quality factors above 10 billion. *Nat. Phys.* **2022**, *18*, 436−441.
(27) Fedorov, S. A.; Engelsen, N. J.; Ghadimi, A. H.; Bereyhi, M. J.; Schilling, R.; Wilson, D. J.; Kippenberg, T. J. Generalized dissipation dilution in strained mechanical resonators. *Phys. Rev. B* **2019**, *99*, No. 054107.
(28) Ferrari, A. C.; Bonaccorso, F.; Fal'ko, V.; Novoselov, K. S.; Roche, S.; Bøggild, P.; Borini, S.; Koppens, F. H. L.; Palermo, V.; Pugno, N.; Garrido, J. A.; Sordan, R.; Bianco, A.; Ballerini, L.; Prato, M.; Lidorikis, E.; Kivioja, J.; Marinelli, C.; Ryhänen, T.; Morpurgo, A.; et al. Science and technology roadmap for graphene, related two-dimensional crystals, and hybrid systems. *Nanoscale* **2015**, *7*, 4598−4810.
(29) Chen, C.; Rosenblatt, S.; Bolotin, K. I.; Kalb, W.; Kim, P.; Kymissis, I.; Stormer, H. L.; Heinz, T. F.; Hone, J. Performance of monolayer graphene nanomechanical resonators with electrical readout. *Nat. Nanotechnol.* **2009**, *4*, 861−867.
(30) Steeneken, P. G.; Dolleman, R. J.; Davidovikj, D.; Alijani, F.; van der Zant, H. S. Dynamics of 2D material membranes. *2D Mater.* **2021**, *8*, No. 042001.
(31) Xu, B.; Zhang, P.; Zhu, J.; Liu, Z.; Eichler, A.; Zheng, X.-Q.; Lee, J.; Dash, A.; More, S.; Wu, S.; Wang, Y.; Jia, H.; Naik, A.; Bachtold, A.; Yang, R.; Feng, P. X.-L.; Wang, Z. Nanomechanical Resonators: Toward Atomic Scale. *ACS Nano* **2022**, *16*, 15545−15585.

https://doi.org/10.1021/acsaelm.4c01261
ACS Appl. Electron. Mater. 2024, 6, 7898−7905

(32) Montblanch, A. R.-P.; Barbone, M.; Aharonovich, I.; Atatüre, M.; Ferrari, A. C. Layered materials as a platform for quantum technologies. *Nat. Nanotechnol.* **2023**, *18*, 555−571.
(33) Agarwal, M. K.; Wani, P. A. Growth conditions and crystal structure parameters of layer compounds in the series Mo1-xWxSe2. *Mater. Res. Bull.* **1979**, *14*, 825−830.
(34) Villanueva, L. G.; Schmid, S. Evidence of surface loss as ubiquitous limiting damping mechanism in SiN micro- and nanomechanical resonators. *Phys. Rev. Lett.* **2014**, *113*, No. 227201.
(35) Jensen, K.; Kim, K.; Zettl, A. An atomic-resolution nanomechanical mass sensor. *Nat. Nanotechnol.* **2008**, *3*, 533−537.
(36) Lemme, M. C.; Wagner, S.; Lee, K.; Fan, X.; Verbiest, G. J.; Wittmann, S.; Lukas, S.; Dolleman, R. J.; Niklaus, F.; van der Zant, H. S. J.; Duesberg, G. S.; Steeneken, P. G. Nanoelectromechanical Sensors Based on Suspended 2D Materials. *Research* **2023**, *2020*, No. 8748602.
(37) Awschalom, D.; Berggren, K. K.; Bernien, H.; Bhave, S.; Carr, L. D.; Davids, P.; Economou, S. E.; Englund, D.; Faraon, A.; Fejer, M.; Guha, S.; Gustafsson, M. V.; Hu, E.; Jiang, L.; Kim, J.; Korzh, B.; Kumar, P.; Kwiat, P. G.; Lončar, M.; Lukin, M. D.; et al. Development of Quantum Interconnects (QuICs) for Next-Generation Information Technologies. *PRX Quantum* **2021**, *2*, No. 017002.
(38) Abdi, M.; Hwang, M. J.; Aghtar, M.; Plenio, M. B. Spin-Mechanical Scheme with Color Centers in Hexagonal Boron Nitride Membranes. *Phys. Rev. Lett.* **2017**, *119*, No. 233602.
(39) Yildirim, T.; Zhang, L.; Neupane, G. P.; Chen, S.; Zhang, J.; Yan, H.; Hasan, M. M.; Yoshikawa, G.; Lu, Y. Towards future physics and applications via two-dimensional material NEMS resonators. *Nanoscale* **2020**, *12*, 22366−22385.
(40) Verbridge, S. S.; Parpia, J. M.; Reichenbach, R. B.; Bellan, L. M.; Craighead, H. G. High quality factor resonance at room temperature with nanostrings under high tensile stress. *J. Appl. Phys.* **2006**, *99*, No. 124304.
(41) Ovartchaiyapong, P.; Pascal, L. M. A.; Myers, B. A.; Lauria, P.; Jayich, A. C. B. High quality factor single-crystal diamond mechanical resonators. *Appl. Phys. Lett.* **2012**, *101*, No. 163505.
(42) Bereyhi, M. J.; Arabmoheghi, A.; Beccari, A.; Fedorov, S. A.; Huang, G.; Kippenberg, T. J.; Engelsen, N. J. Perimeter Modes of Nanomechanical Resonators Exhibit Quality Factors Exceeding 10^9 at Room Temperature. *Phys. Rev. X* **2022**, *12*, No. 021036.
(43) Yan, T.; Qiao, X.; Liu, X.; Tan, P.; Zhang, X. Photoluminescence properties and exciton dynamics in monolayer WSe2. *Appl. Phys. Lett.* **2014**, *105*, No. 101901.
(44) Liu, F.; Wu, W.; Bai, Y.; Chae, S. H.; Li, Q.; Wang, J.; Hone, J.; Zhu, X.-Y. Disassembling 2D van der Waals crystals into macroscopic monolayers and reassembling into artificial lattices. *Science* **2020**, *367*, 903−906.
(45) Purdie, D. G.; Pugno, N. M.; Taniguchi, T.; Watanabe, K.; Ferrari, A. C.; Lombardo, A. Cleaning interfaces in layered materials heterostructures. *Nat. Commun.* **2018**, *9*, No. 5387.
(46) Park, K.-D.; Jiang, T.; Clark, G.; Xu, X.; Raschke, M. B. Radiative control of dark excitons at room temperature by nano-optical antenna-tip Purcell effect. *Nat. Nanotechnol.* **2018**, *13*, 59−64.
(47) Luo, X.; Zhao, Y.; Zhang, J.; Toh, M.; Kloc, C.; Xiong, Q.; Quek, S. Y. Effects of lower symmetry and dimensionality on Raman spectra in two-dimensional WSe_2. *Phys. Rev. B* **2013**, *88*, No. 195313.
(48) Cartamil-Bueno, S. J.; Cavalieri, M.; Wang, R.; Houri, S.; Hofmann, S.; van der Zant, H. S. Mechanical characterization and cleaning of CVD single-layer h-BN resonators. *npj 2D Mater. Appl.* **2017**, *1*, No. 16.
(49) Velický, M.; Donnelly, G. E.; Hendren, W. R.; McFarland, S.; Scullion, D.; DeBenedetti, W. J.; Correa, G. C.; Han, Y.; Wain, A. J.; Hines, M. A.; Muller, D. A.; Novoselov, K. S.; Abruña, H. D.; Bowman, R. M.; Santos, E. J.; Huang, F. Mechanism of gold-assisted exfoliation of centimeter-sized transition-metal dichalcogenide monolayers. *ACS Nano* **2018**, *12*, 10463−10472.
(50) Lin, Y. C.; Jin, C.; Lee, J. C.; Jen, S. F.; Suenaga, K.; Chiu, P. W. Clean transfer of graphene for isolation and suspension. *ACS Nano* **2011**, *5*, 2362−2368.
(51) Zhuang, B.; Li, S.; Li, S.; Yin, J. Ways to eliminate PMMA residues on graphene — superclean graphene. *Carbon* **2021**, *173*, 609−636.
(52) Jain, A.; Bharadwaj, P.; Heeg, S.; Parzefall, M.; Taniguchi, T.; Watanabe, K.; Novotny, L. Minimizing residues and strain in 2D materials transferred from PDMS. *Nanotechnology* **2018**, *29*, No. 265203.
(53) Barg, A.; Tsaturyan, Y.; Belhage, E.; Nielsen, W. H.; Møller, C. B.; Schliesser, A. Measuring and imaging nanomechanical motion with laser light. *Appl. Phys. B* **2017**, *123*, No. 8.
(54) Hauer, B. D.; Doolin, C.; Beach, K. S.; Davis, J. P. A general procedure for thermomechanical calibration of nano/micro-mechanical resonators. *Ann. Phys.* **2013**, *339*, 181−207.
(55) Albrecht, T. R.; Grütter, P.; Horne, D.; Rugar, D. Frequency modulation detection using high-Q cantilevers for enhanced force microscope sensitivity. *J. Appl. Phys.* **1991**, *69*, 668−673.
(56) *Encyclopedia of Systems Biology*, 1st ed.; Dubitzky, W.; Wolkenhauer, O.; Cho, K.-H.; Yokota, H., Eds.; Springer, 2013.
(57) Kramer, E.; van Dorp, J.; van Leeuwen, R.; Venstra, W. J. Strain-dependent damping in nanomechanical resonators from thin MoS2 crystals. *Appl. Phys. Lett.* **2015**, *107*, No. 091903.
(58) Barton, R. A.; Ilic, B.; van der Zande, A. M.; Whitney, W. S.; McEuen, P. L.; Parpia, J. M.; Craighead, H. G. High, Size-Dependent Quality Factor in an Array of Graphene Mechanical Resonators. *Nano Lett.* **2011**, *11*, 1232−1236.
(59) Zhang, R.; Koutsos, V.; Cheung, R. Elastic properties of suspended multilayer WSe2. *Appl. Phys. Lett.* **2016**, *108*, No. 042104.
(60) Peng, M.; Cheng, J.; Zheng, X.; Ma, J.; Feng, Z.; Sun, X. 2D-materials-integrated optoelectromechanics: recent progress and future perspectives. *Rep. Prog. Phys.* **2023**, *86*, No. 026402.

https://doi.org/10.1021/acsaelm.4c01261
ACS Appl. Electron. Mater. 2024, 6, 7898−7905